CERN/LHCC/2007-001
LHCC I-016
12 January, 2007

Zero Degree Calorimeters for ATLAS

ATLAS Collaboration

Letter of Intent

ATLAS Collaboration

Argentina
University of Buenos Aires, Buenos Aires
National University of La Plata, La Plata

Armenia
Yerevan Physics Institute, Yerevan

Australia
Research Centre for High Energy Physics, Melbourne University, Melbourne
University of Sydney, Sydney

Austria
Institut für Experimentalphysik der Leopold-Franzens-Universität Innsbruck, Innsbruck
Fachhochschule Wiener Neustadt (FHWN), Wiener Neustadt

Azerbaijan Republic
Institute of Physics, Azerbaijan Academy of Science, Baku

Republic of Belarus
Institute of Physics, National Academy of Science, Minsk
National Centre for Particle and High Energy Physics, Minsk

Brazil
Universidade Federal do Rio de Janeiro, COPPE/EE/IF, Rio de Janeiro

Canada
University of Alberta, Edmonton
University of Carleton, Carleton
Group of Particle Physics, University of Montreal, Montreal
Department of Physics, McGill University, Montreal
University of Regina, Regina
Simon Fraser University, Burnaby, BC
Department of Physics, University of Toronto, Toronto
TRIUMF, Vancouver
Department of Physics, University of British Columbia, Vancouver
University of Victoria, Victoria

CERN
European Laboratory for Particle Physics (CERN), Geneva

China
Joint Cluster formed by IHEP Beijing, Nanjing, Shandong and USTC Hefei

Czech Republic
Academy of Sciences of the Czech Republic, Institute of Physics and Institute for Computer Science, Prague
Charles University in Prague, Faculty of Mathematics and Physics, Prague
Czech Technical University in Prague, Faculty of Nuclear Sciences and Physical Engineering, Faculty of Mechanical Engineering, Prague

Denmark
Niels Bohr Institute, University of Copenhagen, Copenhagen

France
Laboratoire d'Annecy-le-Vieux de Physique des Particules (LAPP), IN2P3-CNRS, Annecy-le-Vieux
Laboratoire de Physique Corpusculaire, Université Blaise Pascal, IN2P3-CNRS, Clermont-Ferrand
Laboratoire de Physique Subatomique et de Cosmologie de Grenoble (LPSC), IN2P3-CNRS-Université Joseph Fourier, Grenoble
Centre de Physique des Particules de Marseille, IN2P3-CNRS, Marseille
Laboratoire de l'Accélérateur Linéaire, IN2P3-CNRS, Orsay
LPNHE, Universités de Paris VI et VII, IN2P3-CNRS, Paris
Commisariat à l'Energie Atomique (CEA), DSM/DAPNIA, Centre d'Etudes de Saclay, Gif-sur-Yvette

Georgia
Institute of Physics of the Georgian Academy of Sciences and Tbilisi State University, Tbilisi

Germany
Physikalisches Institut, Universität Bonn, Bonn
Institut für Physik, Universität Dortmund, Dortmund
Technical University Dresden, Dresden
Fakultät für Physik, Albert-Ludwigs-Universität, Freiburg
Justus-Liebig-University Giessen, Giessen
Institut für Hochenergiephysik der Universität Heidelberg, Heidelberg
Humboldt Universität Berlin, Institut für Physik, Berlin
Institut für Physik, Universität Mainz, Mainz
Lehrstuhl für Informatik V, Universität Mannheim, Mannheim
Sektion Physik, Ludwig-Maximilian-Universität München, Munich
Fachbereich Physik, Universität Siegen, Siegen
Fachbereich Physik, Bergische Universität, Wuppertal
DESY, Hamburg und Zeuthen
Max-Planck-Institut für Physik, Munich

Greece
Athens National Technical University, Athens

Athens University, Athens
University of Thessaloniki, High Energy Physics Dept. and Dept. of Mechanical Engineering, Thessaloniki

Israel
Department of Physics, Technion, Haifa
School of Physics, Tel-Aviv University, Tel-Aviv
Department of Particle Physics, The Weizmann Institute of Science, Rehovot

Italy
Dipartimento di Fisica dell'Università di Bologna and I.N.F.N., Bologna
Dipartimento di Fisica dell'Università della Calabria e I.N.F.N., Cosenza
Laboratori Nazionali di Frascati dell'I.N.F.N., Frascati
Dipartimento di Fisica dell'Università di Genova and I.N.F.N., Genova
Dipartimento di Fisica dell'Università di Lecce e I.N.F.N., Lecce
Dipartimento di Fisica dell'Università di Milano e I.N.F.N., Milan
Dipartimento di Scienze Fisiche, Università di Napoli 'Federico II' e I.N.F.N., Naples
Dipartimento di Fisica Nucleare e Teorica dell'Università di Pavia e I.N.F.N., Pavia
Dipartimento di Fisica dell'Università di Pisa e I.N.F.N., Pisa
Dipartimento di Fisica dell'Università di Roma I 'La Sapienza' and I.N.F.N., Roma
Dipartimento di Fisica dell'Università di Roma II 'Tor Vergata' and I.N.F.N., Roma
Dipartimento di Fisica dell'Università di Roma III 'Roma Tre' and I.N.F.N., Roma
Dipartimento di Fisica dell'Università di Udine e I.N.F.N., Udine

Japan
Hiroshima Institute of Technology, Hiroshima
Department of Physics, Hiroshima University, Higashi-Hiroshima
KEK, High Energy Accelerator Research Organisation, Tsukuba
Kobe University, Kobe
Department of Physics, Kyoto University, Kyoto
Kyoto University of Education, Kyoto
Nagasaki Institute of Applied Science, Nagasaki
Nagoya University, Nagoya
Faculty of Science, Okayama University, Okayama
Osaka University, Osaka
Department of Computer Science, Ritsumeikan University, Kusatsu
Faculty of Science, Shinshu University, Matsumoto
International Center for Elementary Particle Physics, University of Tokyo, Tokyo
Physics Department, Tokyo Metropolitan University, Tokyo
Institute of Physics, University of Tsukuba, Tsukuba

Morocco
Faculté des Sciences Aïn Chock, Université Hassan II, Casablanca, and Université Mohamed V, Rabat

Netherlands
FOM - Institute SAF NIKHEF and University of Amsterdam/NIKHEF
Radboud University Nijmegen and NIKHEF, Nijmegen

Norway
University of Bergen, Bergen
University of Oslo, Oslo

Poland
Institute of Nuclear Physics (IFJ PAN), Polish Academy of Sciences, Cracow
Faculty of Physics and Nuclear Techniques of the University of Mining and Metallurgy, Cracow

Portugal
Laboratório de Instrumentação e Física Experimental de Partículas (LIP), Lisbon, in collaboration with: University of Lisboa, University of Coimbra, University Católica-Figueira da Foz and University Nova de Lisboa

Romania
National Institute for Physics and Nuclear Engineering, Institute of Atomic Physics, Bucharest

Russia
Institute for Theoretical and Experimental Physics, Moscow
P.N. Lebedev Institute of Physics, Moscow
Moscow Engineering and Physics Institute (MEPhI), Moscow
Moscow State University, Moscow
Budker Institute of Nuclear Physics (BINP), Novosibirsk
State Research Center of the Russian Federation - Institute for High Energy Physics (IHEP), Protvino
Petersburg Nuclear Physics Institute, St. Petersburg

JINR
Joint Institute for Nuclear Research, Dubna

Serbia
Institute of Physics, University of Belgrade, Belgrade

Slovak Republic
Bratislava University, Bratislava, and Institute of Experimental Physics of the Slovak Academy of Sciences, Kosice

Slovenia
Jozef Stefan Institute and Department of Physics, University of Ljubljana, Ljubljana

Spain
Institut de Física d'Altes Energies (IFAE), Universitat Autònoma de Barcelona, Bellaterra (Barcelona)
Physics Department, Universidad Autónoma de Madrid, Madrid
Instituto de Física Corpuscular (IFIC), Centro Mixto Universidad de Valencia - CSIC, Valencia and Instituto de Microelectrónica de Barcelona, Bellaterra (Barcelona)

Sweden
Fysika institutionen, Lunds universitet, Lund
Royal Institute of Technology (KTH), Stockholm
Stockholm University, Stockholm
Uppsala University, Department of Radiation Sciences, Uppsala

Switzerland
Laboratory for High Energy Physics, University of Bern, Bern
Section de Physique, Université de Genève, Geneva

Taiwan
Academia Sinica, Taipei

Turkey
Department of Physics, Ankara University, Ankara
Department of Physics, Bogaziçi University, Istanbul

United Kingdom
School of Physics and Astronomy, The University of Birmingham, Birmingham
Cavendish Laboratory, Cambridge University, Cambridge
Department of Physics and Astronomy, University of Glasgow, Glasgow
Department of Physics, Lancaster University, Lancaster
University of Liverpool, Liverpool
Department of Physics, Queen Mary and Westfield College, University of London, London
Department of Physics, Royal Holloway and Bedford New College, Egham
Department of Physics and Astronomy, University College London, London
Department of Physics and Astronomy, University of Manchester, Manchester
Department of Physics, Oxford University, Oxford
Rutherford Appleton Laboratory, Chilton, Didcot
Department of Physics, University of Sheffield, Sheffield

United States of America
State University of New York at Albany, New York
Argonne National Laboratory, Argonne, Illinois
University of Arizona, Tucson, Arizona
Department of Physics, The University of Texas at Arlington, Arlington, Texas
Lawrence Berkeley Laboratory and University of California, Berkeley, California
Physics Department of the University of Boston, Boston, Massachusetts

Brandeis University, Department of Physics, Waltham, Massachusetts
Brookhaven National Laboratory (BNL), Upton, New York
University of Chicago, Enrico Fermi Institute, Chicago, Illinois
Nevis Laboratory, Columbia University, Irvington, New York
Department of Physics, Duke University, Durham, North Carolina
Department of Physics, Hampton University, Virginia
Department of Physics, Harvard University, Cambridge, Massachusetts
Indiana University, Bloomington, Indiana
Iowa State University, Ames, Iowa
University of California, Irvine, California
Department of Physics, University of Massachusetts, Amherst
Massachusetts Institute of Technology, Department of Physics, Cambridge, Massachusetts
Michigan State University, Department of Physics and Astronomy, East Lansing, Michigan
University of Michigan, Department of Physics, Ann Arbor, Michigan
Department of Physics, New Mexico University, Albuquerque
New York University, Department of Physics, New York
Ohio State University, Columbus, Ohio
Department of Physics and Astronomy, University of Oklahoma
Oklahoma State University, Oklahoma
University of Oregon, Eugene, Oregon
Department of Physics, University of Pennsylvania, Philadelphia, Pennsylvania
University of Pittsburgh, Pittsburgh, Pennsylvania
Institute for Particle Physics, University of California, Santa Cruz, California
Department of Physics, Southern Methodist University, Dallas, Texas
SLAC, Stanford
State University of New York at Stony Brook, New York
Tufts University, Medford, Massachusetts
High Energy Physics, University of Illinois, Urbana, Illinois
Department of Physics, Department of Mechanical Engineering, University of Washington, Seattle, Washington
Department of Physics, University of Wisconsin, Madison, Wisconsin
Physics Department, University of Yale, New Haven, Connecticut

Contents

Chapter 1

Introduction

We propose to build Zero Degree Calorimeters (ZDCs) for ATLAS. These are compact calorimeters that are located at approximately zero degrees to the incident beams on either side of IP1, 140 m downstream from the IP. They thus observe forward going neutral particles that are produced in heavy ion (HI), pA, or *pp* collisions.

The ZDCs have longitudinal segmentation and position sensitivity. In heavy ion collisions they will measure "spectator" neutrons providing an important handle on Pb-Pb collision centrality and allowing ATLAS to trigger on ultra-peripheral collisions. The proposed ZDCs are versatile devices in that they serve to study heavy ion physics, *pp* physics, and provide a tool to tune both the HI and *pp* beams. They are designed to be as radiation hard as practicable, since the radiation levels in the position of the ZDC are extremely high.

While the ZDC is a physically small device, it occupies a large and critical region of phase space. The ZDC fills the transverse aperture of the neutral particle absorber (TAN), and captures the decay products of π^0 and other particles over as wide a kinematic range as the geometrical constraints of the TAN permit.

Members of ATLAS led the design and construction of the zero-degree calorimeters used by all four experiments at the Relativistic Heavy Ion Collider (RHIC) facility at Brookhaven and have extensive experience in the operation of these detectors for both heavy ion and proton-proton collisions [1]. The RHIC ZDCs proved their merit as an important component of the RHIC program. Originally justified by heavy ion physics, they also were useful for *pp* physics and for beam tuning.

In the following we will expand on the physics potential of the device, will describe the construction of the ZDC in detail, and will address how the ZDC will be integrated in ATLAS.

Chapter 2

ZDC Physics

2.1 The ZDC in Heavy Ion Collisions

The primary role of the ZDC in heavy ion physics (HI) is in event characterization of HI collisions. When heavy ions collide only a portion of the ions overlap and collide. Those nucleons that interact are called "participant" nucleons, and those that travel on essentially unscathed are "spectators". This is depicted in cartoon form in Fig. 2.1. The spectator neutrons, observed by the ZDC, carry the nominal beam energy of 2.75 TeV. Due to Fermi motion of the nucleons in the initial nuclei, their energy has about a 10% dispersion, and their position at the ZDC has an rms 6 mm scatter about the central value. The energy of the spectator neutrons as measured by the ZDC allows us to determine their number. Based on experience with the RHIC ZDCs a 20% energy resolution is sufficient for this task since it allows 1 and 2 neutron peaks to be clearly resolved. The ZDCs can thus determine the participant number in an unbiased way by sampling the spectator neutrons [2]. This can be seen in Fig. 2.2 : a scatter plot of the number of neutrons seen in the ZDC vs. the number of widely scattered particles for RHIC events. Measurement of the number of spectator neutrons is equivalent to measuring the magnitude of the impact parameter or"centrality" of the collision since the more central the collision, the larger the number of widely scattered particles.

The spectator neutrons also receive a small amount of transverse momentum. Their momentum vectors, in combination with those of the incident ions, form a plane - "the reaction plane". At RHIC properties of jets were studied versus their direction with respect to the reaction plane. Since the ZDCs also can measure the transverse position of the spectator neutrons, they can determine the orientation of this reaction plane. We use the first term in the Fourier expansion of the azimuthal distribution of particles in an HI event to describe "directed flow". It is found to increase linearly with rapidity, reaching a maximum in the beam fragmentation region covered by the ZDC. The orientation of the flow and hence the reaction plane is observed by the displacement of the center of gravity of the ZDC energy deposition - a measurement well suited to the ZDC design. There are several advantages to studying particle distributions with respect to the reaction plane as observed by the ZDCs rather than as determined with more central detectors.

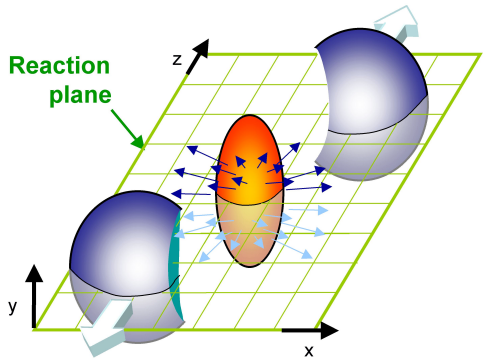

Figure 2.1: Cartoon depicting two colliding heavy ions. Sphere fractions are clusters of spectator nucleons while almond shaped object is cluster of participants.

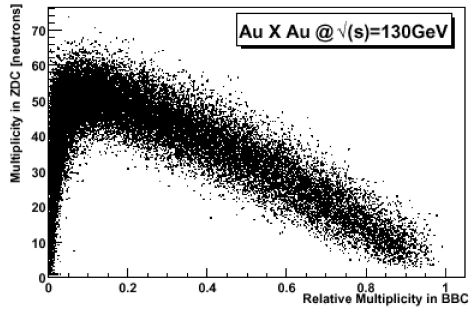

Figure 2.2: The ZDC-measured neutron multiplicity (vertical scale) plotted against the "normalized" charged particle multiplicity in large angle counters (BBCs). These measurements sample the spectator number and participant number respectively and are combined to form an event centrality.

It should be noted that a lack of spectator neutrons can be a result of central collisions or "ultra-peripheral" collisions in which many neutrons remain bound in larger nuclear fragments. It is through observation the central particle multiplicity in the ATLAS inner detector (ID) that this ambiguity can be resolved and the centrality of the event determined.

Since free neutrons are produced at essentially all centralities, and there is negligible probability for the number of neutron spectators to fluctuate to zero, a ZDC coincidence is an ideal minimum bias trigger. As a result at RHIC the ZDC was used as such, and the motivation for this trigger will be more significant at the LHC.

A prerequisite for measuring the modification of jets in heavy ion collisions is the availability of baseline data. The baseline relevant for ATLAS heavy ion runs is pp data taken preferably at $\sqrt{s_{NN}}$=5.5 TeV or p-Pb collisions at the same energy. Alternately by analyzing heavy ion data according to centrality one can express this modification in terms of a ratio - R_{CP} - the ratio of central to peripheral cross sections corrected for the number of binary collisions. Because the ZDC is efficient at all centralities, ZDC trigger data are the best source for peripheral data with well-understood number of binary collisions. The lower energy p-nucleus and p-p reference data, though desirable, may not be available until several years after the first heavy ion measurements.

Finally, the ZDC is needed to tag a wide variety of topics in ultra-peripheral HI collisions such as hard photo-production and quasi elastic vector meson production. In these events there is relatively little central detector activity and a ZDC coincidence is a useful complement to the trigger. The PHENIX detector at RHIC, in measuring ultra-peripheral J/ψ photo-production observed that it is very useful to incorporate

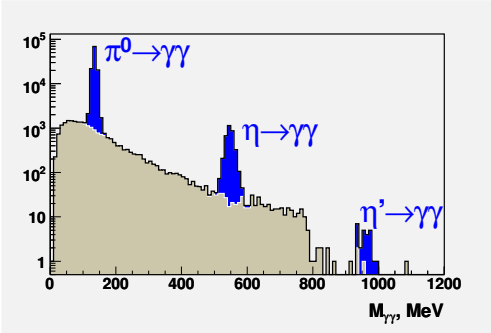

Figure 2.3: Simulated $\gamma\gamma$ mass spectrum from 7 TeV proton on 7 TeV proton production in the forward direction. π^0, η, and η' events are shaded (or in blue).

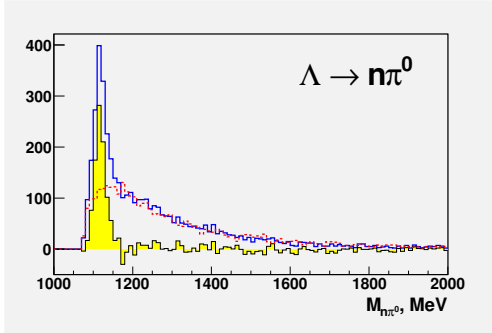

Figure 2.4: $n\gamma\gamma$ mass spectrum from 7 TeV proton on 7 TeV proton production in the forward direction where the decay vertex as determined from $M_{\gamma\gamma} = M_{\pi^0}$ is separated from the interaction point. Solid line is the total spectrum, dashed line is the mixed event background, and shaded (or yellow) histogram is the result (interpreted as $\Lambda \to n\pi^0$ decay) of subtracting background from the total.

one or more neutron tags in the trigger. A recent paper calculates the fraction of hard photoproduction events where additional photon exchanges lead to nuclear breakup. We have incorporated the tagging fraction calculation in Ref. [3] in our rate calculations. This result is confirmed by the PHENIX J/ψ measurement and the PHENIX measurement showed that neutron tagging is essential for designing a low rate trigger [4].

2.2 ZDC p-p capabilities

The neutrons detectable in the ZDC have pseudo rapidity of 8.3 and higher (with a maximum intensity at about 9-10). The Feynman scaling variable, $x_F = 2P_\parallel/\sqrt{s}$, can be measured down to 0.03, and $P_\perp$ in the range from zero to 3.3 GeV/c at the largest x_F, with a resolution of 10% of the range.

In addition to detecting forward going neutrons, the ZDC can detect and reconstruct π^0 and η decaying to $\gamma\gamma$ (Fig. 2.3), $\Lambda \to n\pi^0$ (Fig. 2.4), $\Delta(1234) \to n\pi^0$ (Fig. 2.5), $\Sigma \to \Lambda\gamma$ (Fig. 2.6), and $K^0_S \to \pi^0\pi^0$ (Fig. 2.7) and measure their production cross section and energy and angle within the acceptance and resolution of our detector. These Figures were generated from 10^6 Pythia 6.3 [5] simulations of p-p interactions at $\sqrt{s} = 14$ TeV with a parametrized resolution of the detector as simulated by GEANT.

In Figs. 2.4, 2.5, and 2.6 the signal is extracted from the total spectrum by subtracting a "mixed event background". Mixed event background is manufactured

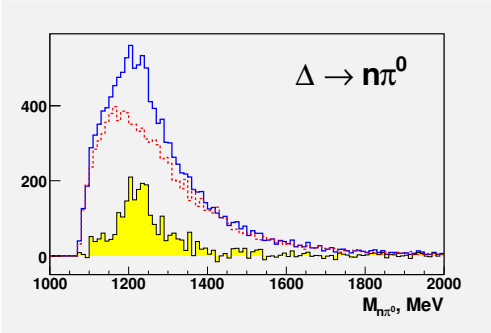

Figure 2.5: $n\gamma\gamma$ mass spectrum from 7 TeV proton on 7 TeV proton production in the forward direction where the decay vertex as determined from $M_{\gamma\gamma} = M_{\pi^0}$ originates at the interaction point. Solid line is the reconstructed effective mass of the n-π^0 pair for all events, dashed line is the mixed event background, and shaded (or yellow) histogram is the result (interpreted as $\Delta \rightarrow n\pi^0$ decay) of subtracting the background from the total.

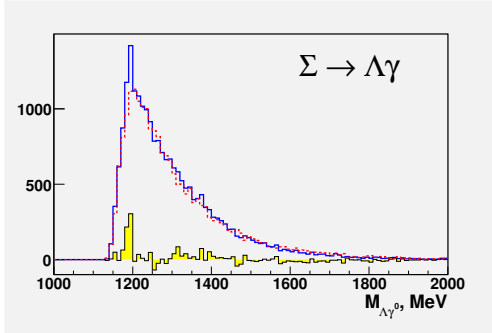

Figure 2.6: $\Lambda\gamma$ effective mass spectrum from 7 TeV proton on 7 TeV proton production in the forward direction. With one hadron and one γ in the detector, it is assumed the hadron is a Λ. Solid line is all events, dashed line is mixed event background, and shaded (or yellow) histogram is the result (interpreted as $\Sigma \rightarrow \Lambda\gamma$ decay)of subtracting the background from the total.

from "pseudo" events by combining particles from several different events. Thus one can observe and subtract uncorrelated particles in the detector - the assumed background. The mixed event normalization may be done using "out-of-signal-peak" events, *e.g.*, events with $M_{n\pi^0} > 1300$ MeV for $\Lambda \rightarrow n\pi^0$ decays. This seems to work for our Pythia events, but must be examined further for validity with real data. We find the number of signal events reconstructed by this method to be consistent with that generated when the required particles go into the detector.

In baryon detection we cannot determine the type of baryon which is observed. For example, according to our Pythia simulation, the number of Λs that reach and interact in the ZDC is expected to be as large as 25% of that of the neutrons. Thus, measurement of the Λs that decay in flight (by observing π^0s that originate downstream from the IP, have an accompanying hadron, and reconstruct to the Λ mass) provides us with an important correction to the neutron cross section result.

Neither can we distinguish between particles and their anti-particles. For understanding cosmic rays (see below) this does not matter since particles and anti-particles will be produced in the same ratios in p-p formation of primary cosmic rays as in p-p collisions at the accelerator.

We do not know cross sections at LHC energies, hence simulation codes like Pythia can only use extrapolations from present energies. The fact that one must rely on such programs with extrapolated parameters over orders of magnitudes to model physics at LHC energies points out the need for a ZDC as described above. Deter-

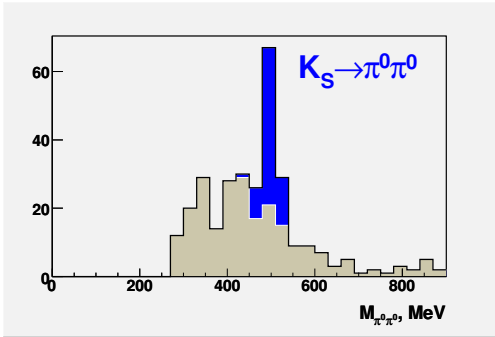

Figure 2.7: $\pi^0\pi^0$ effective mass spectrum from 7 TeV proton on 7 TeV proton production in the forward direction. The peak from K_s^0 can be clearly seen above background of two π^0s

mining production cross sections from such high energy pp collisions will refine the parameterizations (in our case Pythia) and models for high energy processes.

ZDCs are also useful as counters to enhance the capabilities of the central detector, especially for diffractive processes. In such processes forward-going particles are more probable than in hard collisions. Even a small ZDC occupies a significant region of this phase space. In searches for processes where missing energy is expected, a ZDC acts to increase the hermeticity of the larger detector system. An explicit example is seen in searches for an invisible Higgs particle where the Higgs is produced diffractively and decays into unobserved particles. If such events were to occur, QED background to elastic scattering, *e.g.*, $pp \to (p\gamma)(p\gamma)$, would overwhelm an invisible Higgs signal, and a ZDC would go far in its suppression [6].

2.3 Cosmic Ray Physics

While measuring cross sections and energy distributions in a new energy domain is inherently of value, a ZDC at the LHC is particularly useful for understanding the initiation of primary cosmic ray showers by high energy protons [7, 8]. At the LHC the proton energy is about 10^{17}eV in one of the proton's rest frame. This energy is of particular interest in the study of cosmic rays since it is just above the "knee" in the cosmic ray energy spectrum. Measurements in this region will give clues to understanding the physical processes at play in the formation of primary cosmic rays.

It is interesting to note that at high energy colliders the acceptance of the detectors extends over a limited range in pseudo rapidity ($|\eta|$ is usually less than 5, ATLAS is 4.9) and is concentrated on hard scattering in the central region. Cosmic ray showers are mostly initiated in a more forward direction with soft scattering. A ZDC measuring forward particle production cross sections with kinematic precision presents a unique opportunity to make measurements in a region where primary cosmic ray studies have had none. Cross section measurements in this direction and at LHC energies will bear on cosmic ray production as protons strike the upper atmosphere, and will increase understanding of the early generation of particle production in air showers.

The ZDC design can determine the kinematics and production cross sections for forward-going neutral pions, kaons, and eta mesons. There are no data on light meson production from protons at LHC energies such as can be provided by the ZDC.

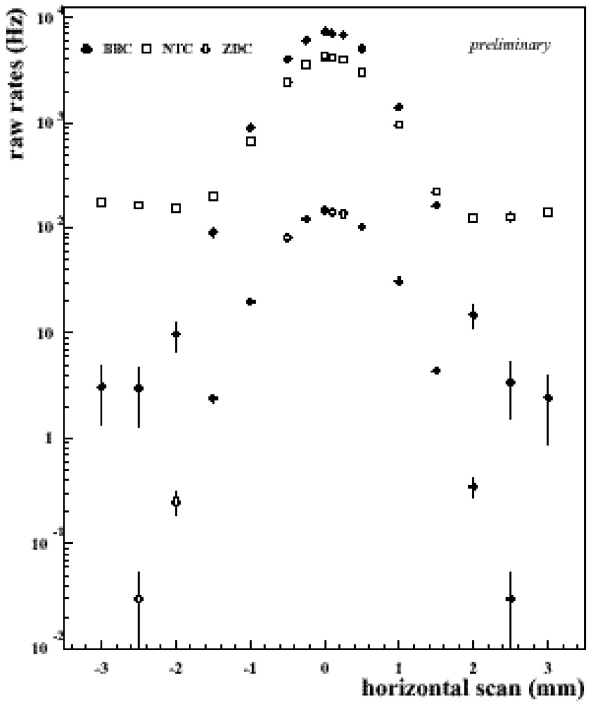

Figure 2.8: Vernier scan rates at RHIC versus beam displacement from coincidences of 3 different detectors. The ZDC-ZDC rates are roughly 2 orders of magnitude lower than the wide counter (BBC) rate but apparently background-free over several orders of magnitude.

2.4 ZDC as an Aid to Beam Tuning and Luminosity Monitoring

The coincidence rate between ZDCs fore and aft of the IP is due only to beam-beam collisions. On the other hand, the particle production rate in other parts of the detector, or a coincidence rate between a forward detector and other parts of the apparatus can be due to beam-gas or beam halo-wall events. That can be seen in Fig. 2.8 from RHIC *pp* data. This Figure is the result of Van der Meer vernier scans at RHIC. It shows the coincidence rate between particle detectors at wide angles (termed BBC and NTC), and the rate of a ZDC in coincidence with the opposite arm ZDC as the beams are swept through one another. One sees that the ZDC-ZDC rate is background-free over four orders of magnitude, while the other methods have a worse signal to background ratio. In *pp* scattering at LHC we find, from Pythia, the ZDC-ZDC coincidence rate to be 9% of the total inelastic rate. We thus assume that Van der Meer scans will be as useful for *pp* at the LHC as it was for *pp* at RHIC.

Since the timing of the ZDC is about 100 ps, one can locate the longitudinal interaction point of the beams to about 3 cm, independent of the barrel detector. In the early days of machine operation it can be quite useful to determine this quantity without relying on the operation of the rest of ATLAS.

The ZDC could provide a useful diagnostic for beam tuning since it can measure the longitudinal position of the interaction point. It can also aid in determining the 150 μrad crossing angle of the beams. Transversely scanning one beam across the other can result in a longitudinal displacement of the interaction point. At RHIC this displacement was used as a check on the crossing angle (which was nominally

0°). The ZDC can also be used to observe structure in the beam such as satellite bunches through ZDC timing information.

2.5 ZDC as a Subsystem of ATLAS

The ZDCs would be run as a subsystem of ATLAS, and as such would allow correlation of forward particle production with those particles observed in the main ATLAS detector. For diffractive processes the ZDCs would be most useful, and would serve as detectors to add to the hermetic nature of the facility. While their resolution will eventually deteriorate due to radiation (see Chapter 5 - Radiation Considerations), they will serve as an adjunct to ATLAS in detecting neutral particles in the forward direction for some time after the start of high luminosity operation.

In Heavy Ion running the ZDCs have proven to be a valuable tool in luminosity calibration. Electromagnetic dissociation (EMD) with neutron emission can be reliably determined using the Weizsacker-Williams formalism, and the effective cross section for ZDC minimum bias trigger coincidences has been calculated for both RHIC Au-Au and LHC Pb-Pb collisions [9]. With RHIC data it was shown that EMD events can also be identified [10] and used to provide an independent luminosity calibration to about 5%.

For p-p collisions, while the relevant cross sections have yet to be measured at LHC energies, the ZDCs can provide a stable, low background relative luminosity monitor.

Chapter 3

ZDC Design

3.1 ZDC Location

The ZDCs reside in a slot in the neutral beam absorbers (TAN). Fig. 3.1 schematically shows the location of the TANs and thus the ZDCs. The TAN is located 140 m from the IP, and is required to absorb the flux of forward high energy neutral particles that would otherwise impinge on the twin aperture superconducting beam separation dipoles (D2). The ZDCs are placed in a slot in the TAN that would otherwise contain inert copper bars as shielding, at the point where the beam pipe transitions from one pipe to two. Figure 3.2 shows two configurations of ZDC modules in the TAN. The two configurations are discussed below in section 7.2.

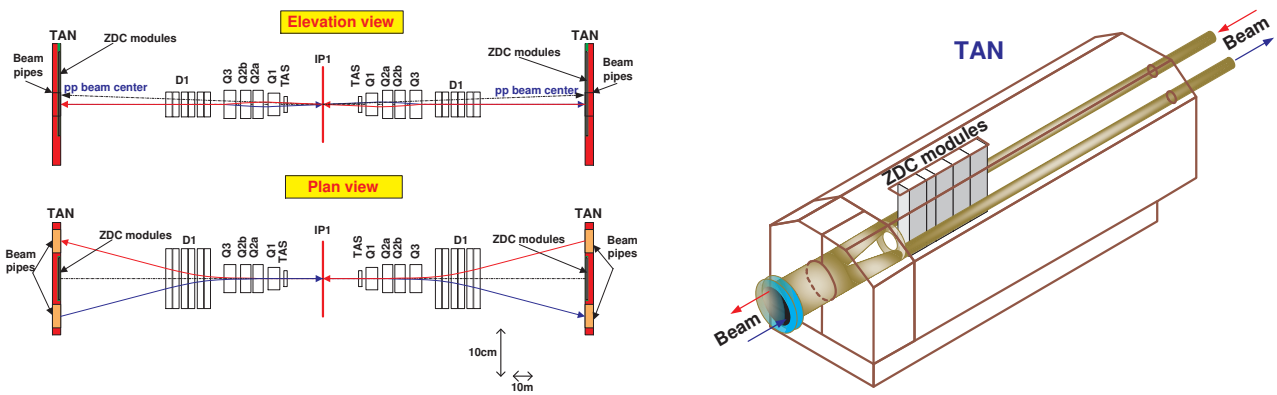

Figure 3.1: LHC beamlines in the region of IP1 showing the location of the ZDCs (left). Transparent view of the TAN showing the beam pipe and location of ZDC modules (right). The TAN is 140 m from the IP.

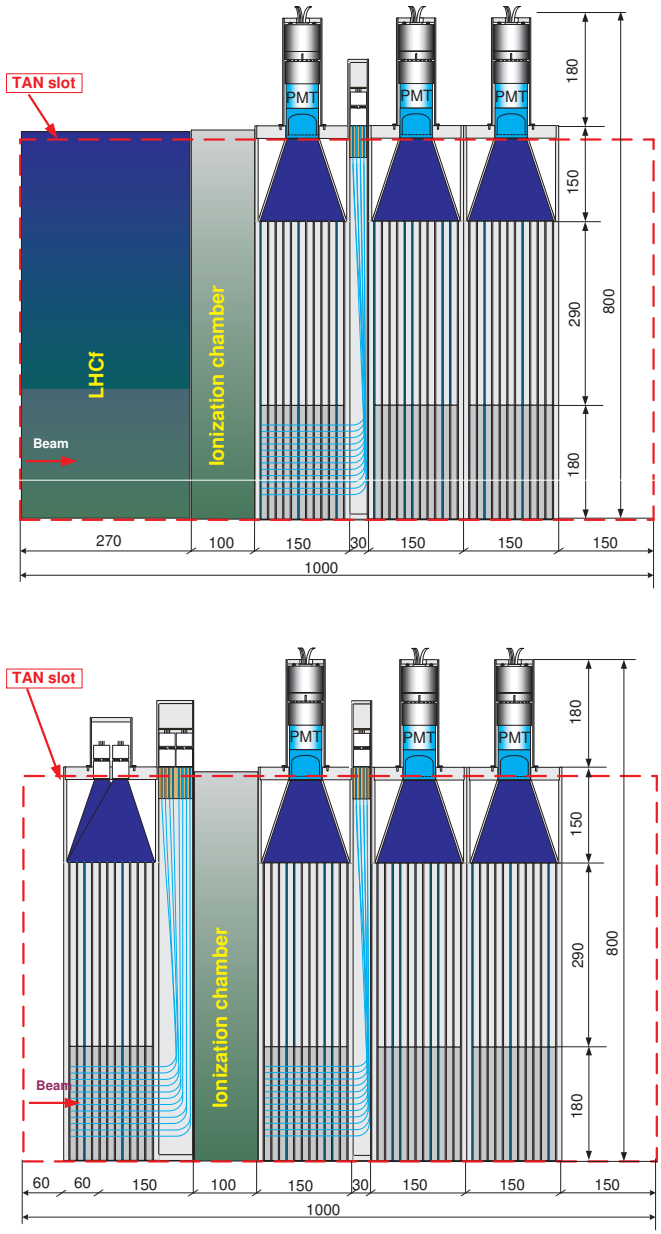

Figure 3.2: ZDC modules as situated in TAN during running for Phase I (top), and Phase II (bottom). The two configurations are discussed in section 7.2

3.2 ZDC Module Description

When the ZDCs are fully installed, there will be four modules - one electromagnetic (EM) module (about $29X_0$ thick) and 3 hadronic modules (each about $1.14\lambda_{int}$ thick) on each arm. In describing the modules we will first describe the EM module since the hadronic modules are similar.

For one arm the EM module is shown in Fig. 3.3. It consists of 11 tungsten (W) plates 91.4 mm wide, 180 mm high, and 10 mm thick in the beam region, with steel plates extending above for 290 mm. Thus the ZDC essentially replaces the Cu bars in the TAN as shielding, and provides the TAN shielding. 1.0 mm diameter Quartz rods penetrate the W plates parallel to the beam in an 8x12 matrix transverse to the beam. At the front end of the module the rods are bent 90° vertically and are viewed from above by multi-anode phototubes (MAPMTs). Thus, Cerenkov light from shower products of incident particles is captured by the quartz rods and observed by the multi-anode tubes. The position of the rods with Cerenkov light signal corresponds to the transverse position of the incident particle, and the intensity of the light reflects the energy of the particle. There are no position sensing rods in the EM module on the other arm.

Between the plates are placed 1.5 mm quartz strips that run vertically and are viewed by photomultiplier tubes from above via air light pipes, or funnels. These strips are actually rows of quartz rods which we term strips to distinguish them from the above described position measuring rods. They are depicted in Fig. 3.4. The purpose of the strips is to get an improved measurement of the incident particle energy over that of the position measuring rods. In the position sensing EM module there are 4 such funnels, side by side, since we expect more than one incident particle per event. In the other EM module there is only one funnel.

The hadronic modules shown in Fig. 3.5 are similar, but while the EM module maps each of the 96 position measuring rods onto one pixel of the multi-anode phototube the hadronic modules maps clusters of four rods onto each pixel, and not all hadronic modules have position sensing rods (there is only one position sensing module per arm). Also, the hadronic modules only have one funnel. Groups of spectator neutrons remain together and appear as a single, large neutron.

We will employ multi-anode phototubes (Hamamatsu R8900-03-16 [11]) for the position sensing function: one hadronic module on each arm with two tubes on each, and one electromagnetic module with six tubes in one arm, while the electromagnetic module in the other arm will have no coordinate readout. On each of the 4 funnels on the E.M. module we will use Hamamatsu R7600U-03 [12]. We will use Photonis XP3292B tubes [13] for single funnels.

Table 3.1 summarizes the ZDC system.

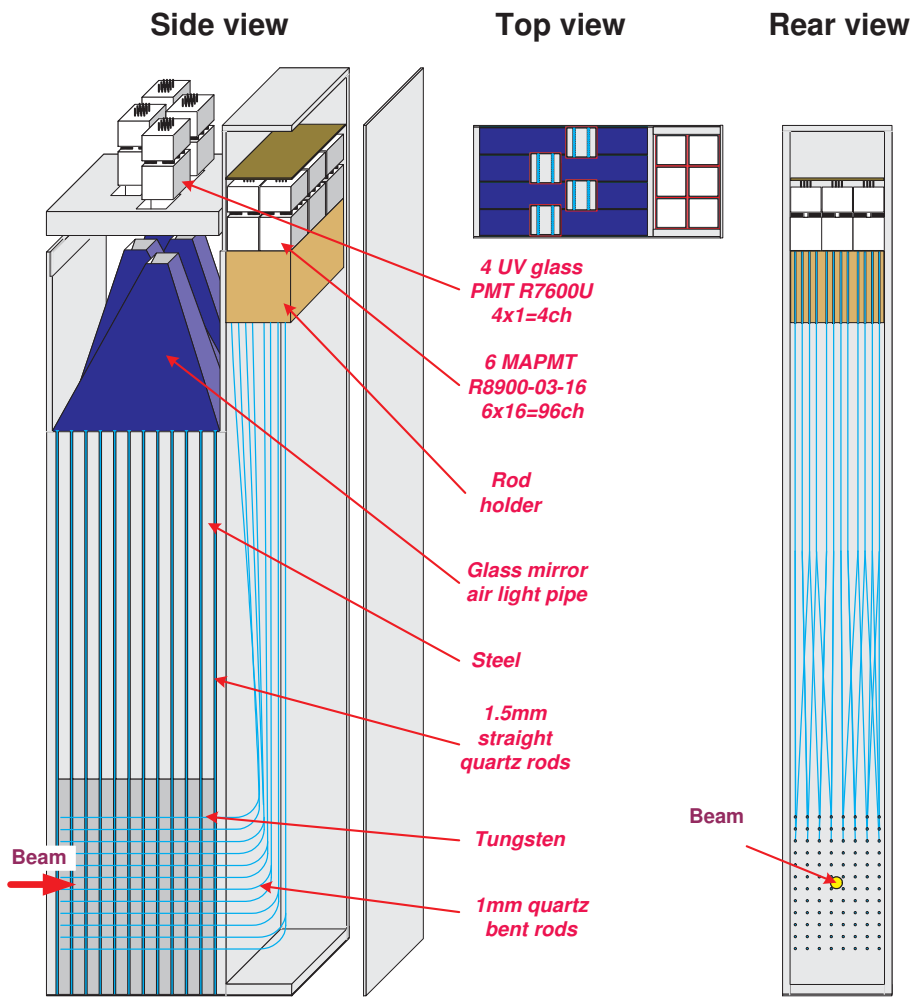

Figure 3.3: Electromagnetic ZDC module. Beam impinges on tungsten plates at bottom of module, and showers. Quartz rods pick up Cerenkov light from the shower and pipe it to multi-anode phototube at top of module. Phototubes measure light from strips through four air light pipe funnels.

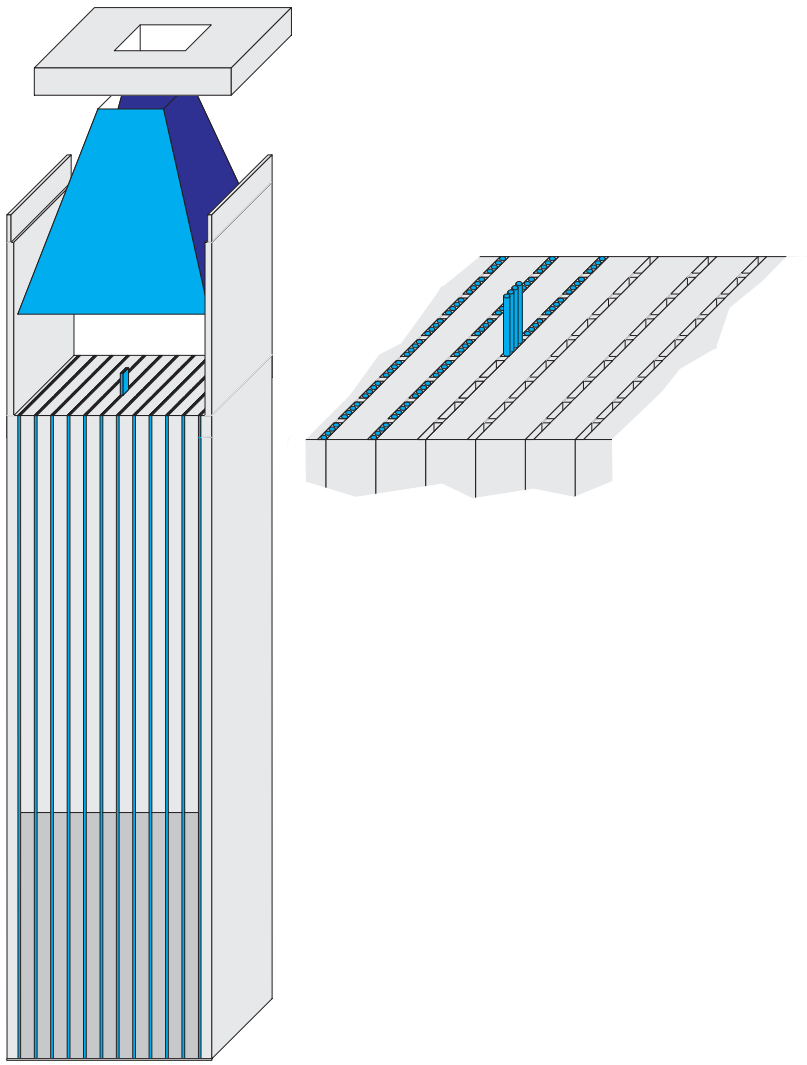

Figure 3.4: Detail of configuration of strips. Left: isometric schematic drawing of the module. Beam enters from the left. Right: isometric drawing of the top of the steel with rods being inserted. Groups of 1.5 mm rods form the strips.

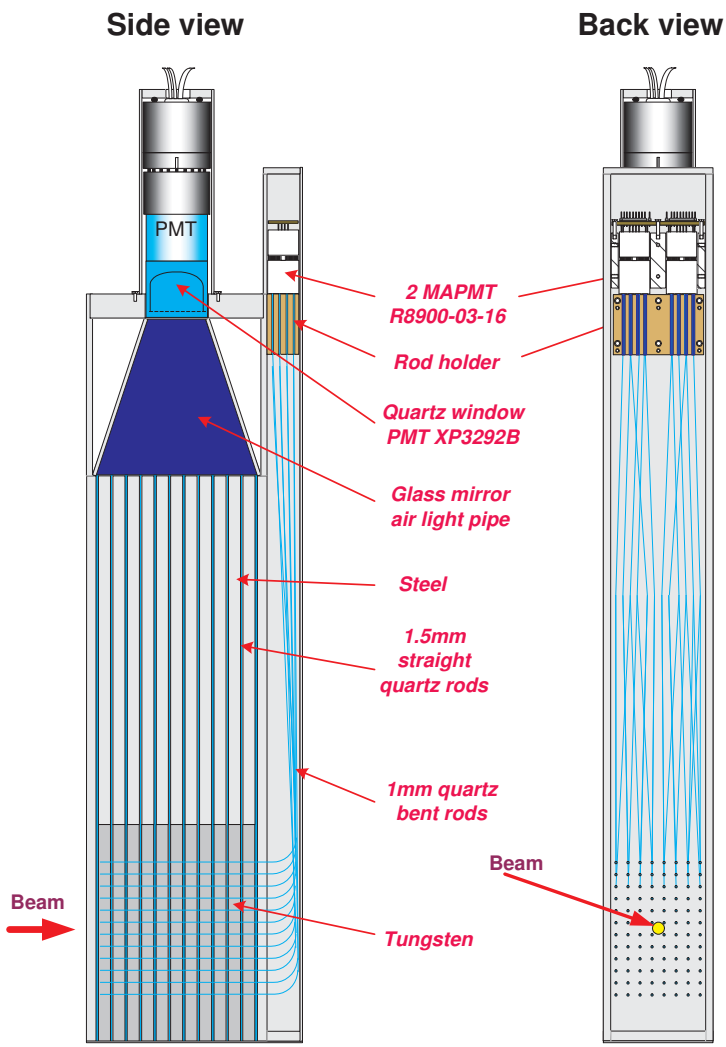

Figure 3.5: Hadronic ZDC module. It has only one PMT viewing the strips, and two MAPMTs viewing the rods.

	Hadronic	Electromagnetic
Number of modules	3 on each arm	1 on each arm
x-y sensing modules	1 on each arm	1 on 1 arm
Energy measuring tubes	3 on each arm	4 on 1 arm, 1 on 1 arm
Tube type	MAPMT: R8900-03-16	Same
	Single channel: XP3292B	Single channel: R7600U
Tot. Int. depth	4.6 λ_{int} on each arm (with EM module)	$29X_0$
Module size (mm)	93.8 wide, 738 high, 150 deep	Same
Tungsten plate size (mm) 11 plates/module	91.4 wide, 180 high, 10 deep	Same
Module weight (kg)	80	Same
Number of strip (1.5 mm) rods	648	Same
Number of pixel (1 mm) rods	96	Same
Number of pixel readout channels	24 (in each arm)	96 (one arm only)

Table 3.1: Summary of ZDC mechanical properties.

3.3 Data Acquisition System

3.3.1 ATLAS Readout Protocols

It is briefly recalled here that ATLAS will operate the TDAQ system with three trigger levels [14, 15]. The first trigger level (L1A) will carry out a rate reduction from 40 MHz down to at most 100 kHz. The second level trigger (LVL2) will reduce the rate by almost two orders of magnitude (3-4 kHz), and the Event Filter (EF) will bring down the recorded rate to the order of 100 Hz.

The ATLAS TDAQ is functionally decomposed into four blocks: the ReadOut subSystem (ROS) including L1A logic, the LVL2 trigger with the the Regions Of Interest (ROI) selection, the Event Builder (EB) and the Event Filter I/O (EF I/O). The ROS is implemented in dedicated hardware while the last three blocks are implemented as processor farms.

The ROS is the main interface between 1600 detector front-end readout links and the high-level trigger farms. This subsystem, on the L1A request ($\sim$ 100 kHz), is responsible for transferring/receiving event fragments (by parallel streams via optical links and RODs - ReadOut Drivers) from Front End Electronics on the detectors (FEEs) to a fragmented PC-based ReadOut Buffer (ROB) subsystem. There the data are stored in the corresponding Readout-Buffer Inputs [16] (ROBIns) which are custom-made core devices of the ROB subsystem and which are capable of handling events at a latency of up to 100 ms, for forwarding for analysis on the LVL2 request or the EB request.

A concurrent part of the ATLAS TDAQ system is a Timing, Trigger and Control (TTC) subsystem [17] that will distribute an LHC clock and trigger signals to the

readout electronics via a special optical link.

3.3.2 ZDC ROS Scheme

In designing the ZDC ROS scheme, we considered the ATLAS TDAQ protocols, the 100 kHz L1A trigger rate, and the demands of the ZDC resolution, among other issues.

The ZDC will also provide an input to the L1A trigger. For HI running this will consist primarily of a 2 arm coincidence with a 1 TeV threshold. For *pp* running it will consist of 1 arm signal above a 1 TeV threshold with a prescale. The current plan is to supply the ZDC triggers as a NIM logic input through the Central Trigger Processor CALibration (CTP_CAL) module, which acts, according to its specifications [18], as a patch panel for NIM inputs from small sub-detector systems [19]. Since the ZDC signals arrive at USA15 1.4 μsec after the crossing, the trigger will fit in the 1.8 μsec time specification for the CTP response.

These considerations lead us to the following specification of the ZDC Readout Scheme:

- The ZDC readout schematic has to include two independent arms under control of a common global L1A-trigger. One arm will include the readout of a combined hadronic/electromagnetic calorimeter (4 ZDC modules) that contains energy/timing PMTs and 24 coordinate PMT channels for one ZDC module. Another arm will include the readout of a combined hadronic/electromagnetic calorimeter that contains 7 energy/timing PMTs, 24 coordinate PMT channels for one ZDC hadronic module and 96 coordinate PMT channels for the ZDC electromagnetic module.

- Due to the high radiation level, digitized electronics could not be located around the ZDC detector. In this case, all analog PMT signals have to be amplified and sent, via coaxial cables, to special ZDC receiver modules in USA15. Here each signal will be processed by a variable gain amplifier/shaper, which will produce a unipolar differential output signal with full length of $\sim$ 60 ns and amplitude within -1 - 0 V range.

- To reach the required energy and timing resolution, all energy/timing PMT signals (11 channels) should be digitized, at least, by 14-bits 80 MHz Wave-Form Digitizer (WFD). The dynamic range of 14 bit is set by requirements of detecting 100 GeV hadrons/photons in *pp* running, and a cluster of up to 70 2.75 TeV (spectator) neutrons in HI running.

- To reach the required coordinate resolution, 144 signals of the coordinate PMTs should be digitized by 14-bits 40 MHz WFD.

- Capability for pile-up analysis of the ZDC response in a time window of 125 - 150 ns ($\sim$5 crossings: 1 past, present and 3 - 4 future) requires a minimal event readout length of 10 - 12 amplitude samples for the ZDC energy/timing channel and 5 - 6 amplitude samples for the ZDC coordinate channel.

- Each WFD channel has to be "dead-time-less" and each WFD channel or group of the WFD channels has to include a WFD pipeline buffer for acquisition and for a parallel readout.

- Each WFD pipeline buffer must include the possibility of reading the digitized data out of a firmware-defined window of the WFD pipeline buffer (under control of an "on-board" FPGA), and to transfer these data to the module's output buffer.

- A shift of this window inside of the WFD pipeline and the depth of the window has to be programmed into the FPGA firmware.

- Each ZDC readout arm has to include one collecting ROD to collect various components of the event format (header, data and trailer) and to build the event fragment according to the ATLAS TDAQ protocols. This ROD must also include the possibility of data transfer to a high level of the ZDC ROS (ROBIn) via a 160 Mbytes optical link - High-speed Optical Link (HOLA)[20]).

- The whole ZDC readout system has to include a special module of the TTC subsystem that will distribute the LHC clock and the L1A trigger signal to every module of the ZDC ROS system via a special bus and will also provide an interface to the ATLAS DCS.

This specification for the ZDC readout leads us to employ electronic modules developed for the ATLAS Level-1 Calorimeter Trigger system (L1Calo) [21]. This system presently is in a production stage and is still available for manufacturing extra modules to meet our needs. We will need three main components of this electronics:

- *The PreProcessor Module (PPM)*: Digitizes, processes 64 analog signals, and identifies them with specific bunch crossings. The 10-bit PPM FADCs will digitize the signals with a sampling frequency of 40 MHz, the same as the bunch crossing rate for the accelerator. The digitized values will be sent then to a custom PreProcessor ASIC (PPrASIC), which has a 2.5 μs pipeline memory to store the raw digitized values and processed data. These data will be readout via an 800 Mbit/s serial optical G-link to the next stage of DAQ upon a L1A trigger.

- *The ROD module*: Receives, formats, compresses, and buffers the PPM transmitted data. The ROD also receives the L1A signal and some data for the ATLAS ROD fragment header via the TTC subsystem. When all required information has been received from the TTC subsystem and PPM, the ROD assembles a complete ZDC event fragment with header, PPM data, and trailer. The ROD then sends the completed fragment to the ZDC ROBIn via a HOLA S-link.

- *The Timing Control Module (TCM)*: Distributes the LHC clock to every PPM or ROD module and provides an interface to the ATLAS DCS, which monitors and controls the operating conditions of the experiment.

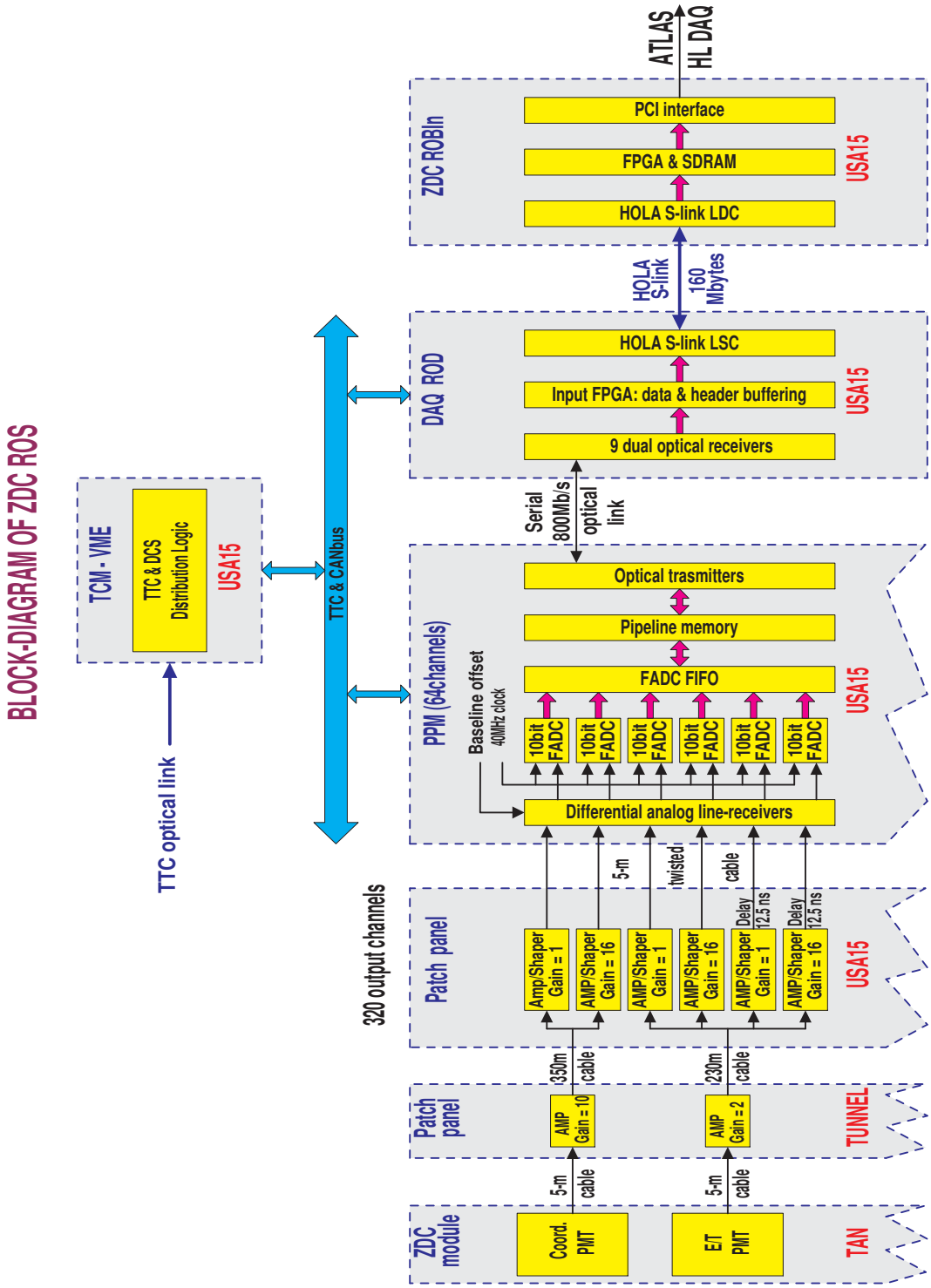

Figure 3.6: A schematic diagram of ZDC ROS. See text for details.

The performance level that can be achieved with this technique is consistent with the ATLAS TDAQ protocols and needs of the ZDC readout.

The block-diagram and schematics of the ZDC readout is shown in Fig. 3.6.

- To achieve the 14-bit resolution for the the coordinate PMTs, the analog signals will be split and amplified into two output differential signals with relative amplification of 1:16. This will be done by special ZDC receiver modules. The subsequent processing of these split signal pairs by pairs of the 10-bit FADCs will emulate the 14-bit signal digitization.

- In reaching the 14-bit 80-MHz scale for the energy/timing PMTs, these analog signals will be split and amplified into two pairs of output differential signals with relative amplification of 1:16. Each pair of split signals will be combined with another pair of split signals, delayed by 12.5 ns, and digitized by a pair of 10 bit FADC. This will emulate 14-bit digitizing at 80-MHz speed.

3.4 Calibration and Monitoring

3.4.1 Flashers

Measurements over a long period of time and the lack of access to the tunnel requires that the PMTs be monitored. Monitoring the gains to an accuracy of $\approx$1% should be sufficient, and can be achieved with a system based on blue LEDs - for instance NICHIA NSPB310A [22]. Using a controllable generator located in USA15, we will excite the LED in the tunnel. On each MAPMT we have reserved one pixel to receive a fiber connected to the LED, and one fiber each will illuminate the single channel PMTs. Tracking the stability of the LEDs will be accomplished by observing their light output with PIN diodes, for instance Hamamatsu S1722-02 [12].

3.4.2 Particles

Full calibration of the ZDC detector begins with determination of the gains in all rod/phototube chains, and measuring shower shape distribution functions, *e.g.* the dependence of single rod amplitudes on the distance to the shower center. These parameters will be permanently monitored during the LHC run. As described in Ref. [23], the full calibration of the EM up to a common normalization coefficient can be done even if the energy and coordinates of the photons are not known.

In *pp* collisions, this preliminary calibration is followed by an *in-situ* calibration using π^0 decay. This method, described in Ref. [24], uses events where there are two and only two photons in the detector. It is based on a previous parametrization of transverse EM shower profiles as observed in the quartz rods. This will be obtained through shower shape analysis at the LHC or at a test beam. The method is an iterative procedure that has been shown by Monte Carlo data to converge.

Once an Electromagnetic module has been calibrated, the hadronic modules will be calibrated. This will be done with $\Lambda \rightarrow \pi^0 n$ events in *pp* collisions. These events

will be selected as having one and only one neutron, and two and only two gammas whose invariant mass is that of a π^0 when the decay vertex is taken as coming from downstream from the IP. Events whose invariant mass is in the peak of the mass spectrum will be chosen as calibration events (see Fig. 2.4). Once the π^0 has been reconstructed the angle between the neutron and π^0 trajectories is known, and we will use the method of Ref. [24], assuming the event was caused by a Λ decay, to calibrate the counters.

One might think that having three modules to absorb the full neutron energy in Λ decay would make this method problematical, but as was demonstrated in our test beam run (see section 6) we correctly simulate the distribution of hadronic energy deposited in individual modules for different amounts of material in front of those modules. Again, this procedure has been demonstrated to work with Monte Carlo data.

When the collider switches to heavy ions, peripheral ion collisions will provide a sample of mono-energetic neutrons with the beam energy of 2.75 TeV. With these we will have a redundant check of our calibration constants.

As mentioned above, monitoring the gains of the tubes in the ZDC system will be done by flashers. The stability of the gains will also be monitored with single photon distributions. Individual pixel gains differ by factors as large as 2 or 3 within a MAPMT. Once determined in initial calibration, however, these gains are constant relative to one another to one percent as observed at RHIC. They will be monitored with single photon distributions, but only the overall gain of a tube should need adjusting.

Chapter 4

ZDC Performance

4.1 Resolution

We have simulated the spatial and energy resolution of the ZDC system described above. The program we used is based on GEANT plus a program to describe light propagation and attenuation in rods, as well as the response of the phototube. It has reliably reproduced results of measurements of these resolutions for Shashlyk counters for the KOPIO experiment at BNL [25], so we have some faith in its predictive power. Figure 4.1 displays photon and neutron energy resolutions of the ZDC system as described above. Figure 4.2 displays the position resolution for the two. Figure 4.3 shows the time resolution for neutrons. The time resolution for photons is about the same as that of neutrons.

As can be seen, the EM energy resolution of the strip readout settles to about 4%, while that of the hadronic modules (neutrons) is about 20% at 1 TeV. Spatially, the resolution for 1 TeV photons is about 0.5 mm and that for the neutrons is roughly 1 mm. One also sees that the time resolution for neutrons is in the 100 ps range, as is the time resolution for 1 TeV photons. We note that it was with the resolutions of Figs. 4.1, 4.2, and 4.3 that the particle distributions shown above were generated - Figs. 2.3, 2.4, 2.5, 2.6.

As an example of the resolution of a ZDC in heavy ion collisions, Fig. 4.4 shows the sum energy of spectator neutrons as measured by a 3×3 cm^2 area centered on the neutron spectator cluster vs. the known number of spectator neutrons. Several hundred events were generated by HIJING for each particular number of spectators. The 3×3 cm^2 area was chosen on an event by event basis and analyzed to obtain the energy and measured centroid of the cluster of neutrons. The uncertainty in the measured energy is dominated by the fluctuation of the number of participant neutrons impinging on the selected 3×3 matrix for each event and the fluctuations of energy deposited in the module. Clearly in HI events with such large neutron multiplicities our ability to pick out π^0s will be limited, but this is not a major objective for the HI program.

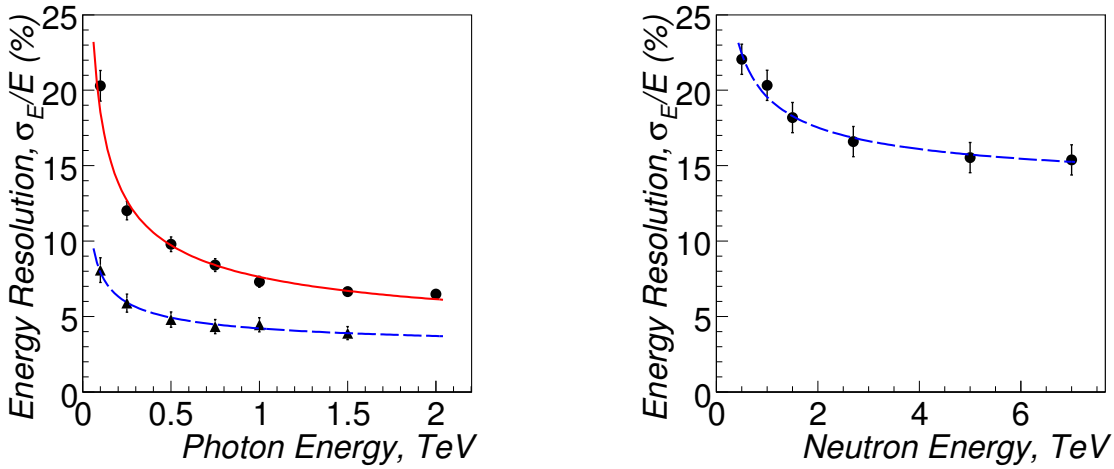

Figure 4.1: ZDC energy resolution for photons (left) and neutrons (right) as a function of energy of the respective particles. Solid (or red) line is for pixel readout and dashed (or blue) lines are for strip readout.

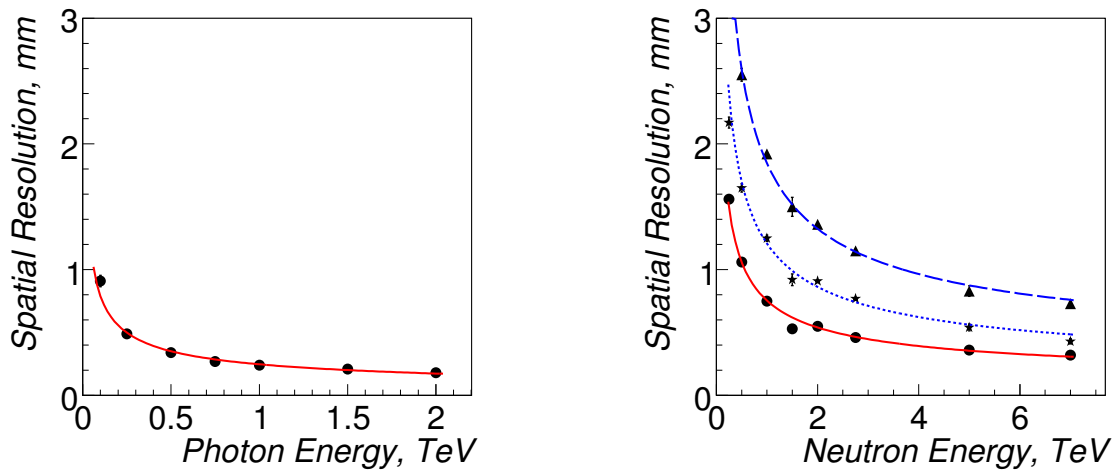

Figure 4.2: ZDC spatial resolution for photons (left) and neutrons (right) as a function of energy of the respective particles. Solid (or red) lines are for electromagnetic ZDC module, dotted line is for hadronic module with fine granularity (one rod per pixel), and dashed line is for hadronic module with coarse granularity (four rods per pixel).

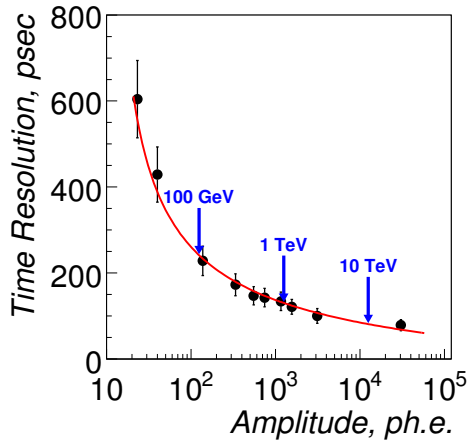

Figure 4.3: ZDC time resolution as a function of number of photoelectrons. Resolution for various neutron energies are shown.

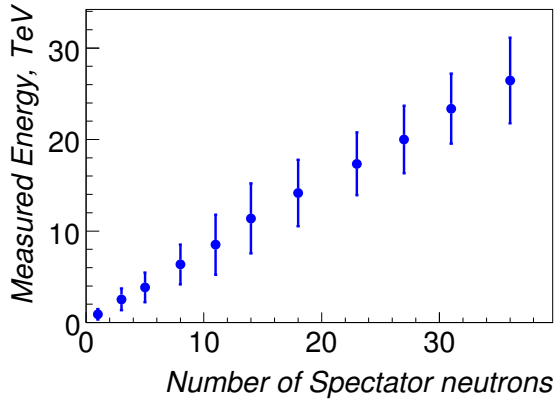

Figure 4.4: Energy measured by a 3×3 cm^2 area centered on the spectator neutron cluster vs. the known number of spectator neutrons in the cluster. Error bars correspond to the rms of measured energy fluctuations. See text for details.

4.2 Geometric Acceptance

The configuration space acceptance at 140 m from the IP is displayed in Fig. 4.5. In this Figure the limitations of all upstream apertures are projected to the 140 m point. We have used the region that is free of the limitations of apertures in our calculations of signal. For background calculations, using GEANT we have allowed particles to scatter off the walls of the limiting components. These calculations have been found to be consistent with those of Ref. [26].

4.3 Kinematic Acceptance

The acceptance for several particle types as a function of x_F, P_T, and $|\eta|$ is displayed in Fig. 4.6. The acceptance of Λs and Δs is similar to that of π^0s. The K_S distributions are quite different from the latter since they involve detection of four gammas as well as decay in flight of the K_S.

4.4 Background

In Fig. 4.7 and Fig. 4.8 we display numbers of neutrons and photons per energy bin as a function of energy for each 7 TeV on 7 TeV *pp* interaction, respectively (note: bin size varies from histogram to histogram). This is shown for several energy ranges of the particles. The color code for these distributions is: red for particles in the

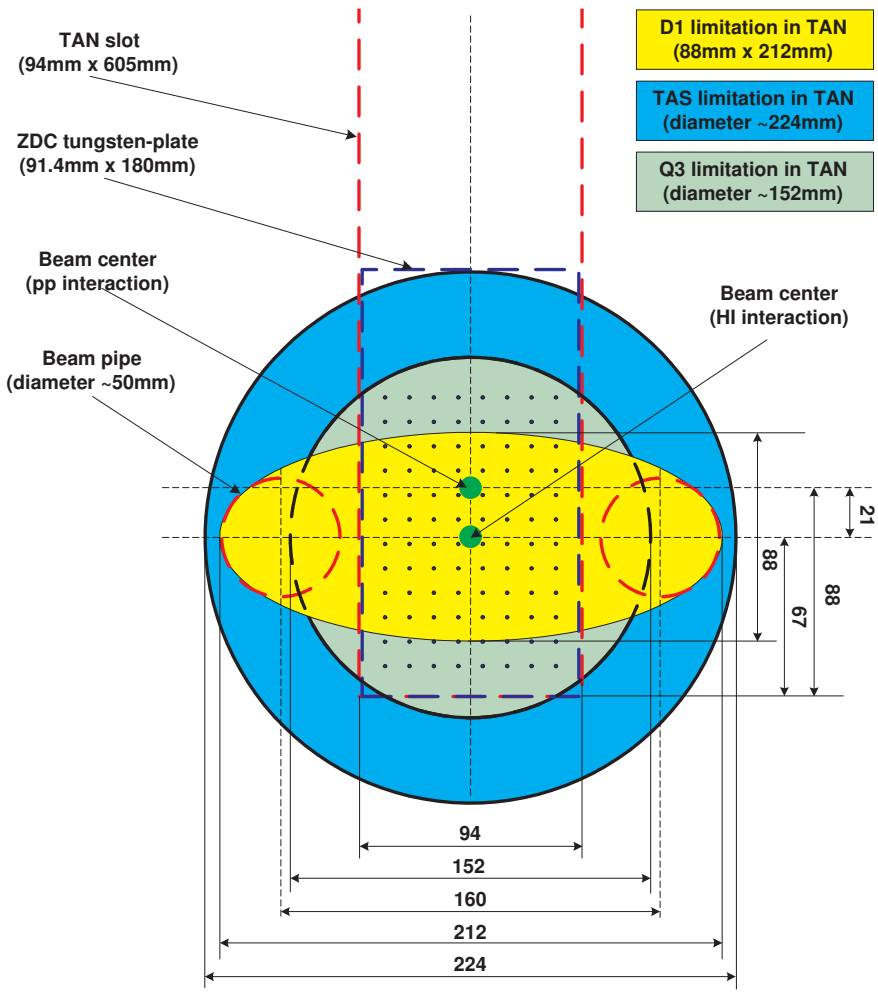

Figure 4.5: Geometrical acceptance of the ZDC at 140 m from the IP. Limiting apertures from upstream elements are projected to the 140 m point and displayed. The horizontal 94 mm by vertical 88 mm region in the center of the Figure is the geometrically unobscured region of the ZDC.

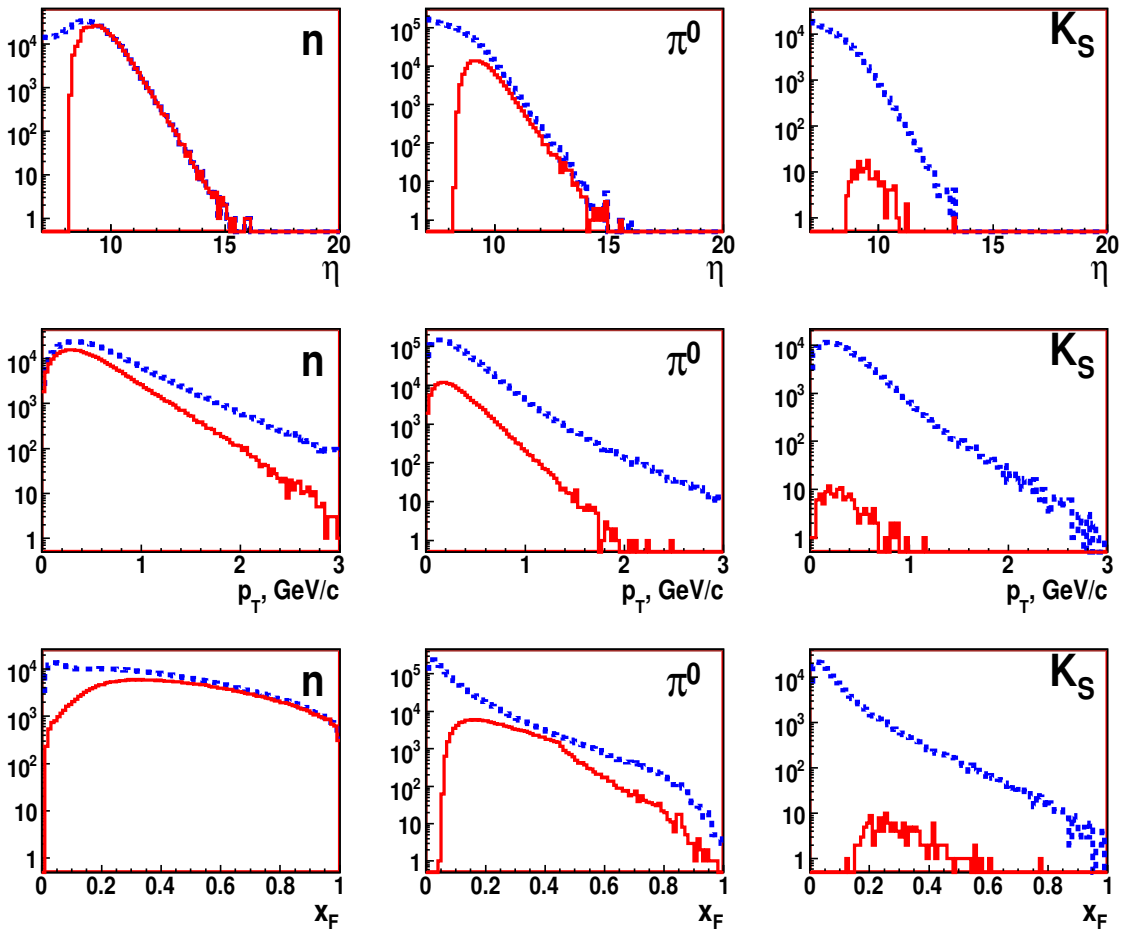

Figure 4.6: Acceptance of a ZDC for n, π^0, and K_S as a function of $|\eta|$, p_T, and x_F. In each distribution the top (Blue) curve is the number of generated events by Pythia, and the bottom (Red) is the number accepted.

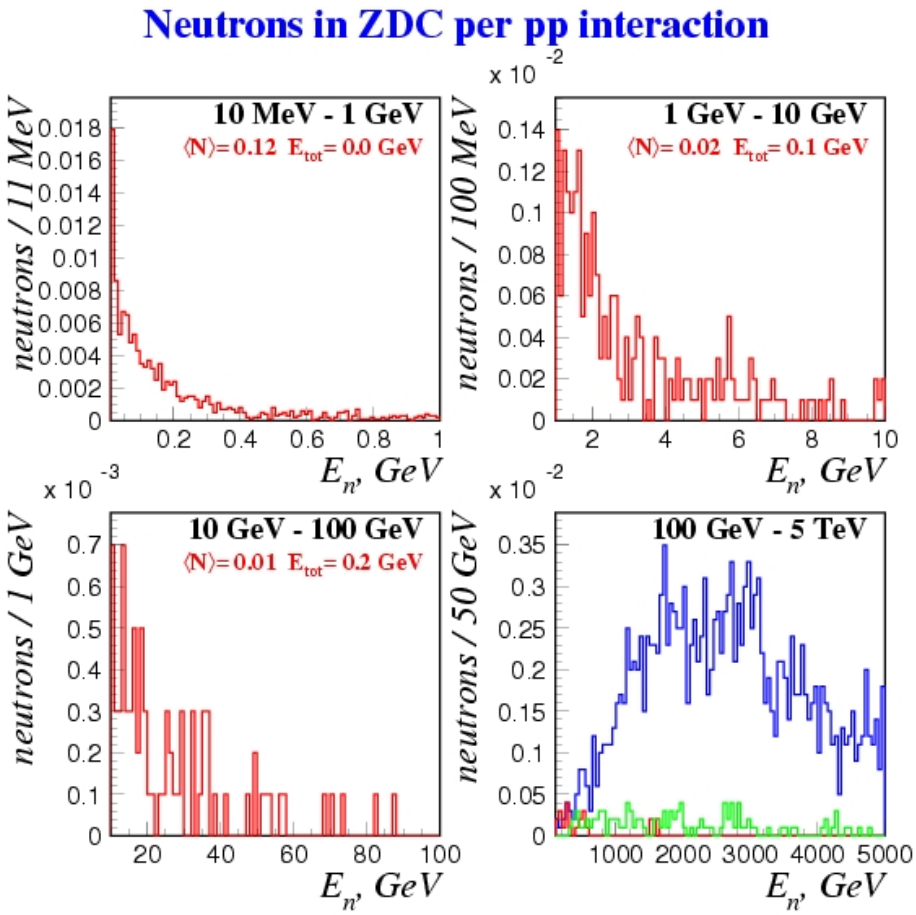

Figure 4.7: Numbers of neutrons per energy bin impinging on the ZDC as a function of energy for each *pp* interaction. Note: the size of energy bins varies between histograms. $\langle N \rangle$ and E_{tot} are for neutron energy ranges within the limits of the respective histograms. See text for details.

ZDC coming from walls of limiting apertures, green for particles coming from decay in flight products, and blue are particles directly from the IP. Also shown in these plots is the average number of the respective particle , $\langle N \rangle$, and the total energy, E_{tot}, of those particles to impinge on the ZDC per *pp* interaction. One sees that all the neutrons hitting the ZDC with an energy above 1 TeV are essentially all coming from the IP. Similarly, all photons above 60 GeV are essentially originating at the IP. Those are our signal particles. The only other particles with such high energies are products of particles which decay in flight.

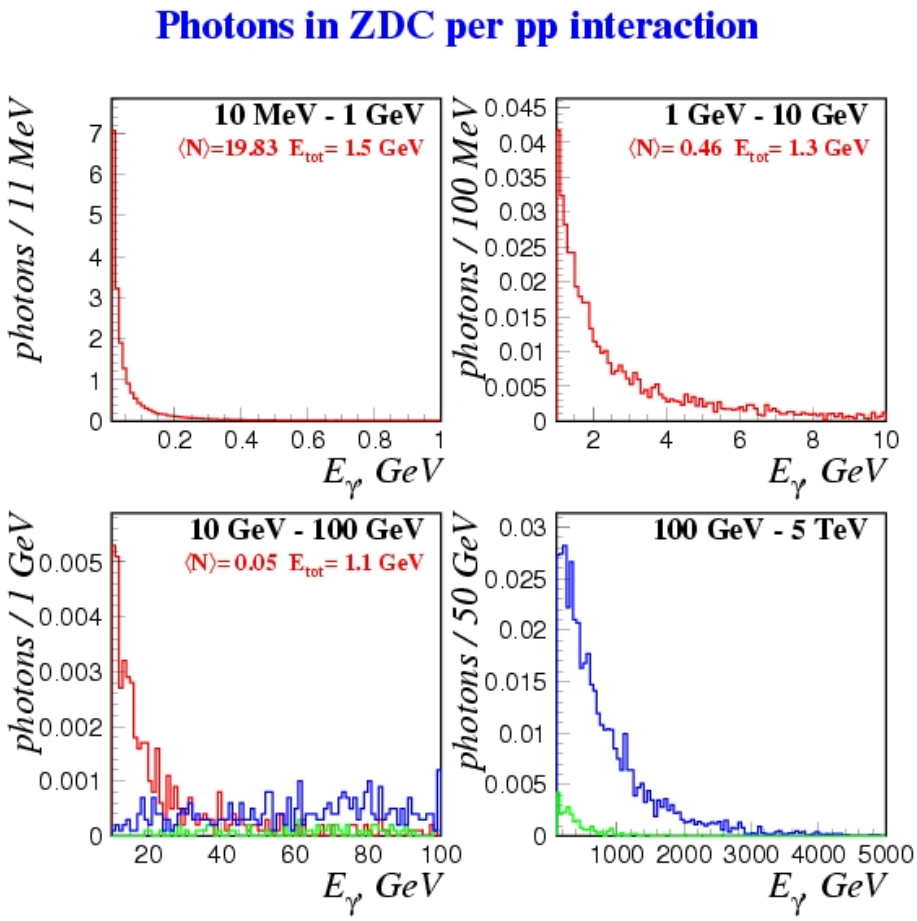

Figure 4.8: Numbers of photons per energy bin impinging on the ZDC as a function of energy for each *pp* interaction. Note: the size of energy bins varies between histograms. $\langle N \rangle$ and E_{tot} are for photon energy ranges within the limits of the respective histograms. See text for details.

Chapter 5

Radiation considerations

It is recognized that the ZDC is situated in one of the regions of highest radiation intensity in the collider complex. We feel that any ZDC operation will be ineffective at the highest machine luminosities. On the other hand, the startup of the machine is planned to be at luminosities that are 10% of the design luminosity, or less. The ZDC can provide a physics program, both in HI and pp, as well as serve as a beam tuning tool, for commissioning at this level and below. In fact, for HI running the luminosities are such that the ZDC can serve indefinitely.

The phototubes are all at a distance of ≈ 550 mm from the center of the beam. In this area the maximum dose for the luminosity of 10^{33} cm^{-2}s^{-1} is expected to be less than 10 krad/yr [26]. For tubes with UV-glass or quartz windows the change in sensitivity from such a dose will be insignificant. The quartz rods are the most vulnerable component of the ZDC to radiation damage. At luminosity of 10^{33} cm^{-2}s^{-1} the region near zero degrees is exposed to ≈ 1.8 Grad per year [26]. To achieve high radiation tolerance for the medium that stimulates and transmits the Cerenkov light in the calorimeter, quartz was selected as the radiating medium. However, there are disparate levels of tolerance published in the literature, and the published levels are for ≈ 300 μm fiber - a fiber diameter which we calculated would give insufficient light in our geometry. We therefore selected unclad 1 mm diameter quartz rods. While they will give sufficient light, the question of radiation tolerance remained. We thus made measurements of our own, and exposed 5 cm long samples of the rods uniformly to an intense 200 MeV proton beam at the Brookhaven Linac Isotope Producer facility (BLIP) in the AGS complex.

It is well known that radiation exposure destroys the UV transmission of quartz before the longer wavelength transmission [27]. For that reason we were interested in the transmission for wavelengths greater than 400 nm. The results of our test are seen in Fig. 5.1. They can be summarized by saying that, for the transmission of light with wavelength longer than 400 nm, the attenuation length of 1 mm diam. rods is reduced from about two meters to about 5-7 cm after an exposure of about 5 Grad.[1] According to our Monte Carlo simulations, this loss of light will degrade the

[1]The break at 6 Grad in Fig. 5.1 occurs because we had quartz samples at different parts of the radiation field. The break is indicative of our uncertainty in the radiation level as a function of position.

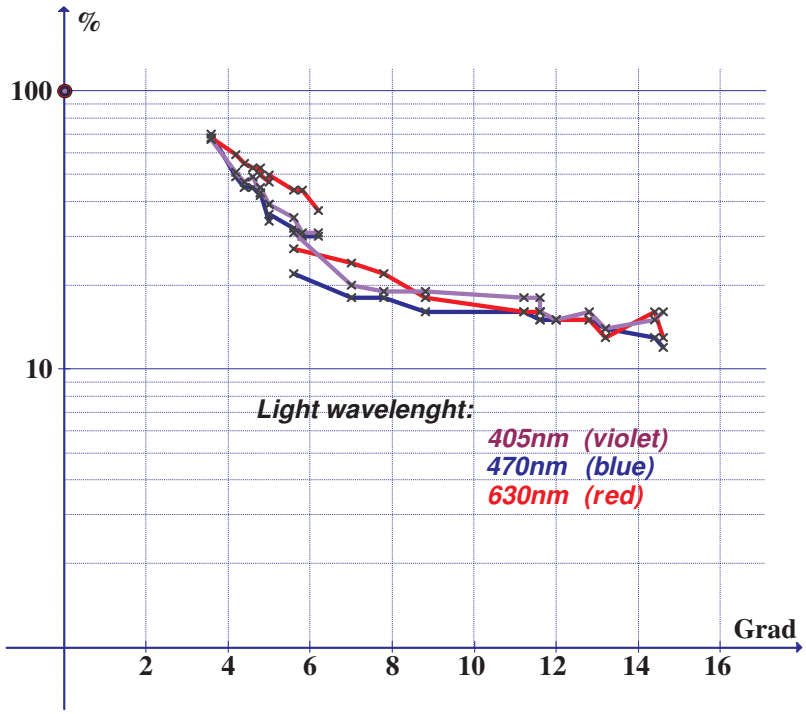

Figure 5.1: Transmission vs dose for 5 cm long 1mm diameter rods.

energy and spatial resolution by no more than 30 - 50%. Because the energy strips are perpendicular to the beam, only a few cm of the strips are exposed to the very high radiation of the beam. Thus the strips will lose resolution more slowly than the rods.

Since the radiation level in the beam region at a luminosity of 10^{34} cm^{-2}s^{-1} will be about 18 Grad/yr [26], our studies indicate that the ZDCs would lose resolution in several months. In the early stages of running the machine, however, the luminosity, and thus radiation levels, will be lower. Scaling the above, we believe that the ZDC will have useful resolution for about 3 years of running at a luminosity of 10^{33} cm^{-2}s^{-1}. As pointed out above, the luminosities for HI running are orders of magnitude lower, 10^{27} cm^{-2}s^{-1}, so the ZDC will be effective correspondingly longer. The effect of variation of the system gain due to radiation will be mitigated with appropriate filtering of the UV light at the phototubes. To protect the ZDCs for heavy ion running, they can be removed for *pp* running with luminosities of order 10^{33} cm^{-2}s^{-1} or greater.

Chapter 6

Test Beam Performance

The test of a prototype of a standard hadronic module took place in the North Area Test Beam at the SPS in a 230 GeV proton beam. The ZDC system is designed to run in a multi TeV beam with several modules in tandem. The test, however, was near the energy threshold of the system for a single module.

Since radiation damage is an issue for quartz in the UV region [27] (see Section 5), we have insured against accepting UV light in this test by using phototubes with Borosilicate windows. A wave length response for our tubes is shown in Fig. 6.1, and is seen to have no efficiency below 300 nm.

As one test we placed different amounts of steel in front of the module to change the depth of hadronic showers in the module. As expected, the distribution of energy deposited in the module varies as a function of this depth. Figure 6.2 shows the results of this test. In it the histograms are the number of events at a given amplitude *vs.* phototube amplitude in ADC counts. Each histogram is for a different amount of steel in front of the module, 0 cm, 10 cm, an 20 cm, respectively. Superimposed on the data are curves of the number of events as predicted by our simulation.

Using the known energy deposited in the module by positrons in a separate run (see below) we were able to determine the amount of light per GeV of energy deposited in a module. That calibration indicates an electromagnetic energy resolution at 230 GeV which is roughly that of our simulation, as shown in Figure 4.1.

The light calibration was made via a special run in which the beam was tuned to enhance the number of positrons relative to the number of hadrons in the beam. The energy spectrum for this run, with no material in front of the module, is seen in Figure 6.3. The curve in this Figure is the simulated energy spectrum for hadrons and muons, and a Gaussian fit to the remaining events - the "positrons". Normalizations were made separately for hadrons and muons. The "positron" Gaussian shape and centroid were determined after subtracting these simulations from the data. It was then assumed that the centroid of the positron distribution was the ADC counts for "positrons" which deposited full beam energy in the module. The amount of light equal to that of the "positrons" was then injected into the phototube, and the number of photoelectrons observed was determined from a statistical analysis. From that analysis we determined the amount of light per TeV of energy deposited in a module (3000 photoelectrons/TeV for electrons), and thus found agreement between

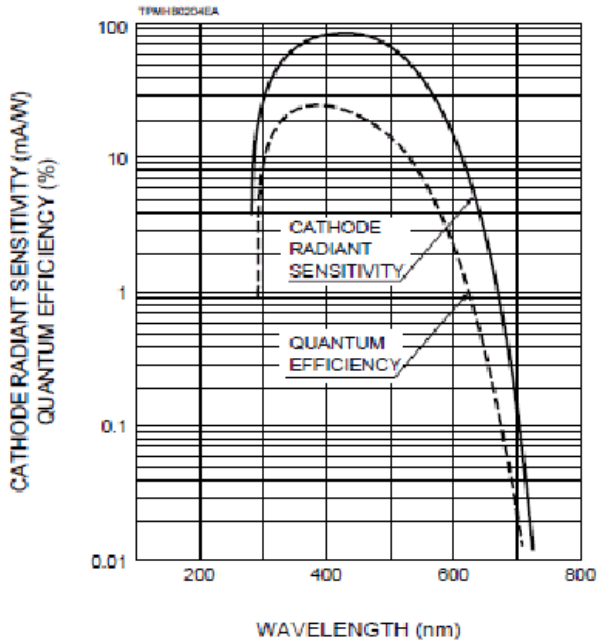

Figure 6.1: Spectral response for the PMT with borosilicate window.

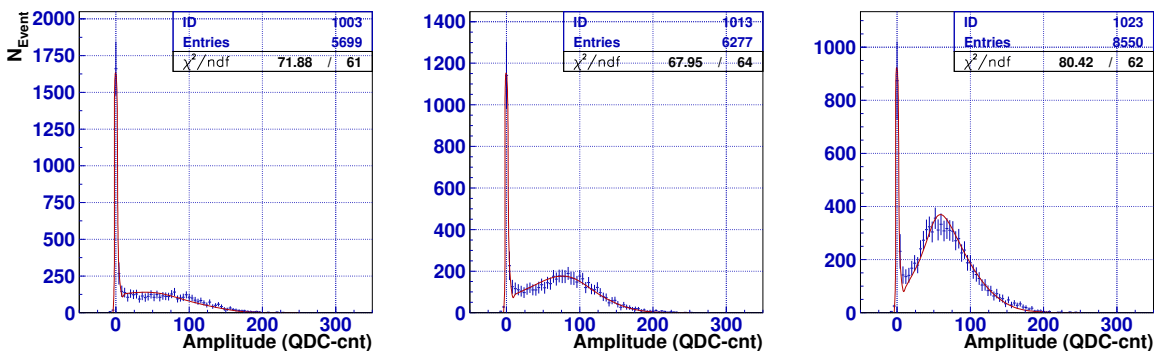

Figure 6.2: ZDC prototype response to 230 GeV/c proton beam. Plots left to right for 0, 10, and 20 cm steel, respectively, in front of module. Curves are simulation.

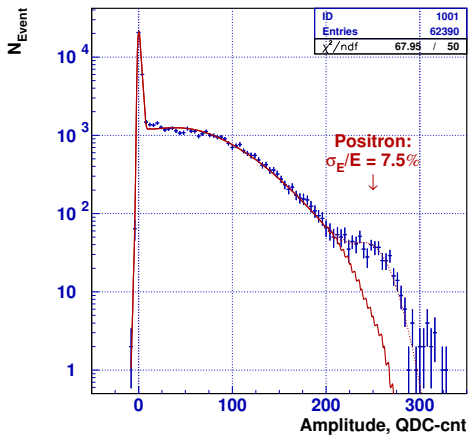

Figure 6.3: ZDC prototype response to 220 GeV/c secondary beam. Bump at high end is assumed to be positrons, and is fit with a Gaussian. See text for details.

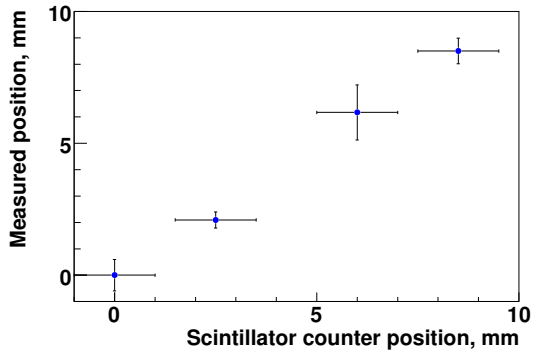

Figure 6.4: Measured beam position versus actual scintillator counter position as measured by a prototype hadronic module.

our experimental resolution and our simulated resolution described above.

Another test was that of spatial resolution sensitivity. With scintillation counters we were able to determine where the beam entered the module to within the width of the counters. We then varied that position by moving the ZDC module vertically. (Position measuring chambers were not available for our short run.) A plot of measured beam position *vs.* the actual position is seen in Fig. 6.4. The relatively low energy of the proton beam and some technical problems during the short test beam run made individual event location problematical. We thus show statistical averages of the centroid of the measured position of the scintillation counters.

Chapter 7

Operation at the LHC

We will be prepared to install the ZDCs before the LHC tunnels are secured for circulating beam at the end of summer, 2007.

7.1 Installation

The ZDC modules are designed to be lowered into the TAN just as are the Cu bars that were originally designed for the TAN. The ZDCs are therefore fully compatible with the CERN installation hardware. Since tungsten has an interaction length about 1.5 times shorter in cm than Cu, the ZDC module in the TAN presents roughly 1.5 times the interacting material as a Cu bar to protect the downstream magnets from radiation.

We have arranged for cables to be run in the tunnel for the ZDC from the TAN to USA15 and have assigned rack space in USA15. Table 7.1 describes these cables. At present the 230 m cables have been run. Plans are in place to run the 350 m cables in a subsequent campaign,

cable use	cable type	no. of cables	length(m)
fast trigger signals	C-50-6-1 50 Ω	4	230
fast signals to WFD's	C-50-3-1 50 Ω	6	230
coordinate readout	C-50-3-1 50 Ω	24	350
extra coordinate readout (1 side)	C-50-3-1 50 Ω	24	350
test signal	C-50-3-1 50 Ω	2	350
PMT HV cable	RG 59 equiv	6	350
extra HV (1-side)	RG 59 equiv	7	350
low voltage	power cable	2	350
EM coordinate readout (1 side)	C-50-3-1 50 Ω	96	350

Table 7.1: Cables from USA15, rack:Y-30.11.A1 to TANs, quantities are per side of IP1.

7.2 Running Plan

We envisage running the ZDC in two phases, termed I and II. In the first phase the EM modules would be replaced with the LHCf experiment. Thus only the three most downstream hadronic modules would initially be installed on each arm. LHCf is "not designed to be a radiation hard detector and so would be removed when the LHCf luminosity exceeds 10^{30} $cm^{-2}s^{-1}$" [28]. In phase II, when the LHCf experiment is removed, we would install our EM modules and run as the radiation levels permit. Fig. 3.2 depicts a view of the TAN for this program. We would also run in the Phase II mode for Heavy Ion running.

Bibliography

[1] S.N. White, Nucl. Inst. Meth. **A417** 1 (1998).

[2] R.J. Glauber, in "Lectures in Theoretical Physics", W.E. Brittin and L.G. Dunham ed. (Interscience, New York) Vol. 1, pg. 315 (1959).

[3] G. Baur *et al.*, Nucl.Phys. **A729** 787, and nucl-th/0307031 (2003).

[4] S. White, "Proceedings of the XIth International Conference on Elastic and Diffractive Scattering", Chateau de Blois, France, May 15 - 20, 2005, and nucl-ex/0510084 (2005).

[5] T. Sjostrand *et al.*, JHEP **05**, 026 (2006).

[6] K. Belotsky *et al.*, "Can an Invisible Higgs Boson be seen via diffraction at the LHC?", Eur. Phys. J. **C36**, 503-507 (2004).

[7] R. Engel, Symposium on Very High Energy Cosmic Ray Interactions,Geneva, Switzerland. hep-ph/021340v1 (2002).

[8] S. Tapprogge,"Prospects of Experimental Measurements at LHC to Better Understand Cosmic Ray Air Showers.", Phys. of At. Nucl. **67** 1 (2004).

[9] A. Baltz *et al.*, Nuc. Inst. and Meth. A417, 1 (1998)

[10] M. Chiu *et al.*, Phys. Rev. Lett 89, 012302 (2002).

[11] Y. Kawasaki *et al.*, Nucl. Inst. and Meth. **A564** 378 (2006).

[12] http://www.hamamatsu.com/

[13] http://www.photonis.com/

[14] ATLAS Collaboration, "Level-1 Trigger. Technical Design Report." http://atlasinfo.cern.ch/Atlas/GROUPS/DAQTRIG/TDR/V1REV1/L1TDR_all.pdf

[15] ATLAS Collaboration. "ATLAS High-Level Trigger, Data Acquisition and Controls. Technical Design Report." http://atlas-proj-hltdaqdcs-tdr.web.cern.ch/atlas-proj-hltdaqdcs-tdr/tdr-v1-r4/PDF/TDR.pdf

[16] ATLAS Collaboration, "The ATLAS ROBIn Prototype", http://robin-group.web.cern.ch/robin-group/ml.html.

[17] R. Spiwoks, "ATLAS TTC Review, 15/05/02", http://atlas.web.cern.ch/Atlas/GROUPS/DAQTRIG/LEVEL1/ctpttc/meet_ttc_150502.pdf

[18] ATLAS Collaboration, "The ATLAS Level-1 Trigger, CTP", http://atlas.web.cern.ch/Atlas/GROUPS/DAQTRIG/LEVEL1/ctpttc/L1CTP.html

[19] ATLAS Collaboration, "The Level One Central Trigger Operation", https://twiki.cern.ch/twiki/bin/view/Atlas/LevelOneCentralTriggerOperation#Trigger_Inputs_to_the_CTP

[20] ATLAS Collaboration, "HOLA - High-speed Optical Link for Atlas, 2.0 Gbps S-LINK LSC and LDC S-LINK Interface", http://www94.web.cern.ch/HSI/s-link/devices/hola/.

[21] ATLAS Collaboration, "The ATLAS Level-1 Calorimeter Trigger", http://hepwww.rl.ac.uk/Atlas-L1/Home.html

[22] http://www.nichia.com/

[23] A.A. Poblaguev, "Shower Reconstruction in the ATLAS ZDC", http://www.phy.bnl.gov/~poblague/zdc/calibration.pdf (2006).

[24] A.A. Poblaguev, "Comment to the ECAL calibration algorithm", http://pubweb.bnl.gov/users/e865/www/calibration_algorithm.pdf (2005).

[25] G.S. Atoian *et al.*, "Development of Shashlyk Calorimeter for KOPIO", Nucl. Inst. Meth. **A531** 476 (2004).

[26] N.V. Mokhov, I.L. Rakhno, J.S. Kerby, J.B. Strait, "Protecting LHC IP1/IP5 Components Against Radiation from Colliding Beam Interactions" (2002).

[27] V. Gavrilov *et al.*, "Study of Quartz Fiber Radiation Hardness", CMS TN-94-324 (1994).

[28] Technical Design Report of the LHCf experiment, CERN-LHCC-2006-004 LHCF-TDR-001 (2006).